

Spin Excitation Spectra of Anisotropic Spin-1/2 Triangular Lattice Heisenberg Antiferromagnets

Runze Chi,^{1,2,*} Yang Liu,^{1,2,*} Yuan Wan,^{1,3} Hai-Jun Liao,^{1,3,†} and T. Xiang^{1,2,4,‡}

¹*Beijing National Laboratory for Condensed Matter Physics and Institute of Physics, Chinese Academy of Sciences, Beijing 100190, China.*

²*School of Physical Sciences, University of Chinese Academy of Sciences, Beijing 100049, China.*

³*Songshan Lake Materials Laboratory, Dongguan, Guangdong 523808, China.*

⁴*Beijing Academy of Quantum Information Sciences, Beijing, 100190, China.*

Investigation of dynamical excitations is difficult but crucial to the understanding of many exotic quantum phenomena discovered in quantum materials. This is particularly true for highly frustrated quantum antiferromagnets whose dynamical properties deviate strongly from theoretical predictions made based on the spin-wave or other approximations. Here we present a large-scale numerical calculation on the dynamical correlation functions of spin-1/2 triangular Heisenberg model using a state-of-the-art tensor network renormalization group method. The calculated results allow us to gain for the first time a comprehensive picture on the nature of spin excitation spectra in this highly frustrated quantum system. It provides a quantitative account for all the key features of the dynamical spectra disclosed by inelastic neutron scattering measurements for Ba₃CoSb₂O₉, revealing the importance of the interplay between low- and high-energy excitations and its renormalization effect to the low-energy magnon bands and high-energy continuums. We identify the longitudinal Higgs modes in the intermediate-energy scale and predict the energy and momentum dependence of spectral functions along the three principal axes that can be verified by polarized neutron scattering experiments. Furthermore, we find that the spin excitation spectra weakly depend on the anisotropic ratio of the antiferromagnetic interaction.

Introduction.—Frustrated quantum magnetism has moved to the forefront of condensed matter physics research. Quite many exotic quantum phenomena driven by the interplay between quantum fluctuations and geometric frustrations, such as quantum spin liquid [1–4] and magnetic monopoles [5], have been discovered in these systems. The spin-1/2 triangular antiferromagnetic Heisenberg model is a prototypical frustrated magnetic system that has been intensively studied for more than four decades [1, 6–9]. While it is now commonly accepted that its ground state is noncollinear 120° magnetic ordered [Fig. 1(a)] [7–9], the physical properties of its excitation states remain elusive.

The linear spin wave theory (LSWT) predicts that there are three magnon excitation modes in the triangular antiferromagnetic Heisenberg model. However, inelastic neutron scattering (INS) measurements on Ba₃CoSb₂O₉ [10–12], which is an excellent realization of the spin-1/2 triangular Heisenberg model [13–16], just observed two branches of magnon excitation modes. More surprisingly, these magnon excitation modes were found to be strongly renormalized around the *M* point [Fig. 1(d)] where the bands bend downward and one of them exhibits a rotonlike minimum. Moreover, two strong dispersive continuums of unknown origin are observed above the low-energy magnon bands [11, 12].

A number of theories have been proposed or invoked to explain the exotic magnetic spectra observed in Ba₃CoSb₂O₉, based either on the multimagnon interactions [10, 12, 17–22] or on the interplay between magnons and fractionalized spinons [23–28]. These theories offered a qualitative explanation to the downward renormaliza-

tion of the three magnon bands. However, a comprehensive understanding to the dynamical spectra in the whole energy range, especially those in the intermediate- and high-energy scales, is still not available. In particular, it is unknown how the spectral weights are transferred to or from low-energy magnon excitations, damped longitudinal Higgs modes and high-energy continuum. In this Letter, we resolve these problems through a thorough investigation on the spin-1/2 triangular Heisenberg model using a state-of-the-art tensor-network renormalization group method [29, 30] in combination with the technique of automatic differentiation [31, 32].

Model and method.—Ba₃CoSb₂O₉ has a highly symmetric hexagonal structure $P6_3/mmc$ [33], and its magnetic Co²⁺ ions with pseudospin 1/2 form a perfect triangular lattice in the *ab* plane. It was proposed that this material presents an ideal realization of the paradigmatic spin-1/2 antiferromagnetic Heisenberg model in two dimensions [13–16],

$$H = J \sum_{\langle ij \rangle} (S_i^x S_j^x + S_i^y S_j^y + \Delta S_i^z S_j^z), \quad (1)$$

where $\langle ij \rangle$ runs over all the nearest-neighbor sites of the triangular lattice, J is the antiferromagnetic coupling constant, and Δ is a parameter measuring anisotropy. In our calculation, we adopt the parameters determined from the magnetization, electronic spin resonance, nuclear magnetic resonance and neutron scattering measurements [11–16, 34], namely, $J = 1.67$ meV and $\Delta = 0.95$. We ignore the interlayer coupling because it is much

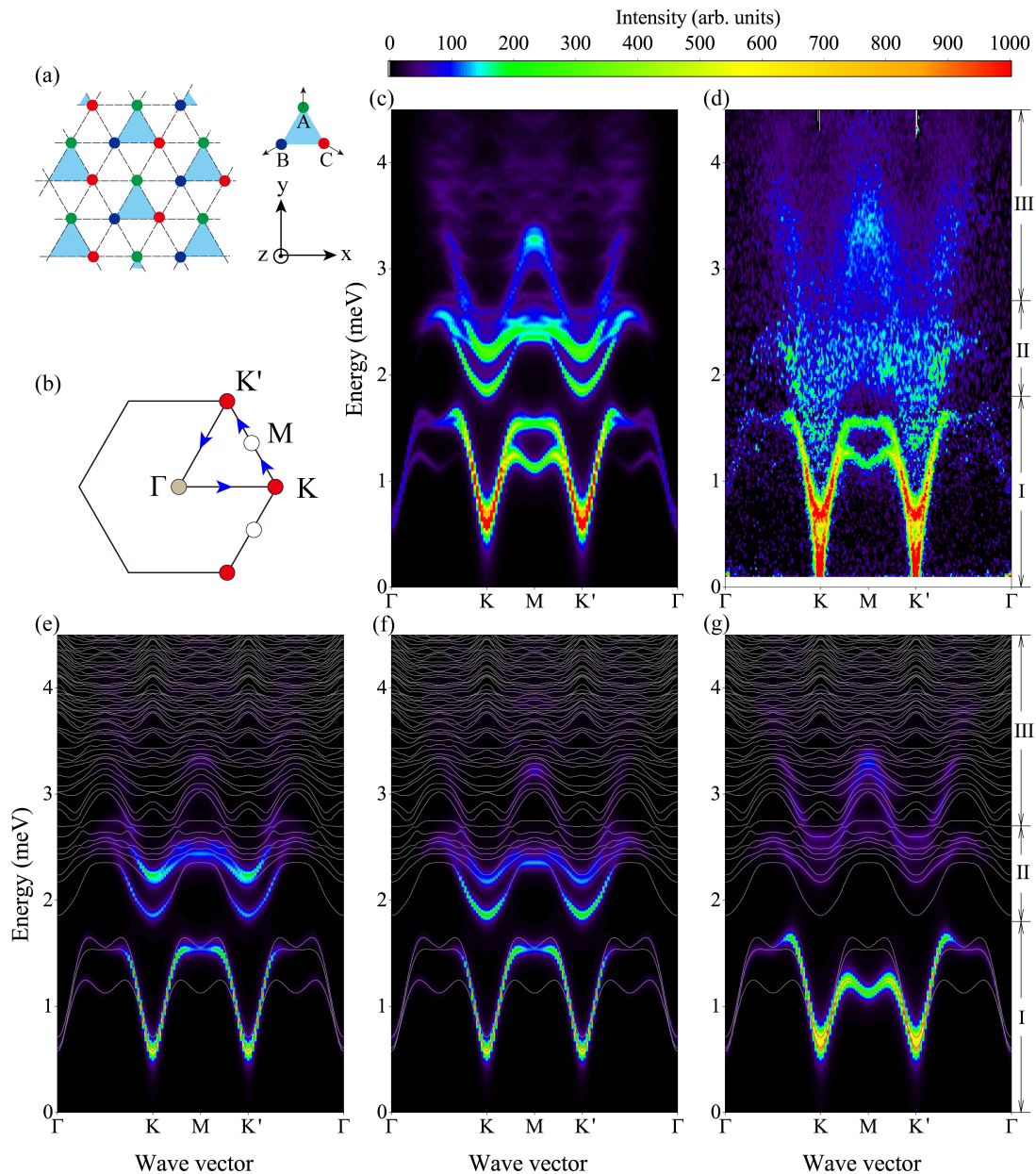


FIG. 1. Comparison between the tensor-network results and the INS measurement data for the dynamical spin structure factors. (a) Triangular lattice and the 120° Néel order in the ground state of the Heisenberg model. The magnetization is ordered along the y -axis direction on sublattice A in the triangular plane. (b) The first Brillouin zone and the momentum path (the arrowed lines) on which the spectral functions are evaluated. (c) The total spectral weight of the dynamical spectral function obtained with the tensor-network method for the easy-plane XXZ model with $J = 1.67$ meV and $\Delta = 0.95$. (d) The INS spectra of $\text{Ba}_3\text{CoSb}_2\text{O}_9$ reproduced using the data published in Supplementary Materials in Ref. [12]. (e)-(g) The spin structure factors along the three principal axes: (e) $S^{xx}(\mathbf{k}, \omega)$, (f) $S^{yy}(\mathbf{k}, \omega)$, and (g) $S^{zz}(\mathbf{k}, \omega)$. Their sum gives the total spectral weight shown in (c). The gray curves show the energy dispersions of the excitation states. The spectra are divided into three stages according to their dispersions: (I) $0 < E < 1.8$ meV, (II) 1.8 meV $< E < 2.7$ meV, and (III) $E > 2.7$ meV.

smaller than the intralayer coupling [13] and the observed magnetic excitations are almost dispersionless along the c axis [11].

We employ the tensor-network formalism to simulate the magnetic excitation spectra of $\text{Ba}_3\text{CoSb}_2\text{O}_9$ under the single-mode approximation [35] in the framework of

projected entangled pair states (PEPS). This approximation was first introduced in the framework of matrix product states by Ostlund and Rommer in one dimension [36, 37]. It was extended to the PEPS presentation in two dimensions by Vanderstraeten *et al.* [38]. Variational optimizations of local tensors are implemented

with the approach of automatic differentiation first introduced to the tensor-network calculations in Ref. [31]. Recently, this approach was extended to the calculation of excitation states in the single-mode approximation of PEPS [32].

The tensor-network calculation is based on the idea of renormalization group. It does not suffer from the notorious minus-sign problem encountered in the quantum Monte Carlo simulations and is applicable to a strongly correlated system with or without quantum or geometric frustrations, such as the model studied here. Moreover, it obeys the sum rule of spin fluctuation (see Fig. S3 in Supplemental Material [39] and Ref. [32]) and can be directly applied to an infinite-lattice system without being bothered by the finite-size effect [39].

Results. — Figure 1(c) shows the intensity of the spin structural function

$$S(\mathbf{k}, \omega) = \sum_{\alpha} S^{\alpha\alpha}(\mathbf{k}, \omega), \quad (\alpha = x, y, z) \quad (2)$$

$$S^{\alpha\beta}(\mathbf{k}, \omega) = \langle 0 | S_{-\mathbf{k}}^{\alpha} \delta(\omega - H + E_0) S_{\mathbf{k}}^{\beta} | 0 \rangle. \quad (3)$$

calculated using the tensor-network methods along a representative path $\Gamma - K - M - K' - \Gamma$ in the Brillouin zone. Here $S^{\alpha\alpha}(\mathbf{k}, \omega)$ is the dynamical spin-spin correlation function along the three axes. Three striking features are revealed in the spectra in different energy ranges.

In the low-energy region, $\omega < 1.8$ meV, two sharp and one weak magnon excitation modes are observed (this can be seen more clearly from Fig. 3). Around the M point, only two sharp excitation modes are visible. The higher-energy mode is almost dispersionless, but the lower one exhibits a pronounced rotonlike minimum. By carefully examining the energy dispersions, shown by the gray lines in Fig. 1(e), we find that these low-energy spectra are contributed by the three magnon bands, consistent with LSWT. However, the overall energy dispersions of these three magnon excitation modes deviate strongly from the LSWT prediction [see Fig. S10 (e)]. The third excitation mode is not clearly seen because the spectral weight of the third band is very small around M . This is consistent with the prediction of a resonating valence bond (RVB) theory [28]. Around the Γ point, the linear magnon dispersions are reproduced, but their intensities are very weak due to the cancellation inside a unit cell. Around the antiferromagnetic vector point K , the spectrum shows a sharp energy dispersion. This dispersion does not go to zero exactly at this point because the long-range correlation of the ground state is terminated by the finite virtual bond dimension of PEPS. Nevertheless, the lowest excitation energy gap at this point, as shown in Fig. S9 in Supplemental Material [39], tends to approach zero with the increase of the bond dimension, as a consequence of Goldstone's theorem. In the intermediate-energy region, $1.8 \text{ meV} < \omega < 2.7 \text{ meV}$, two

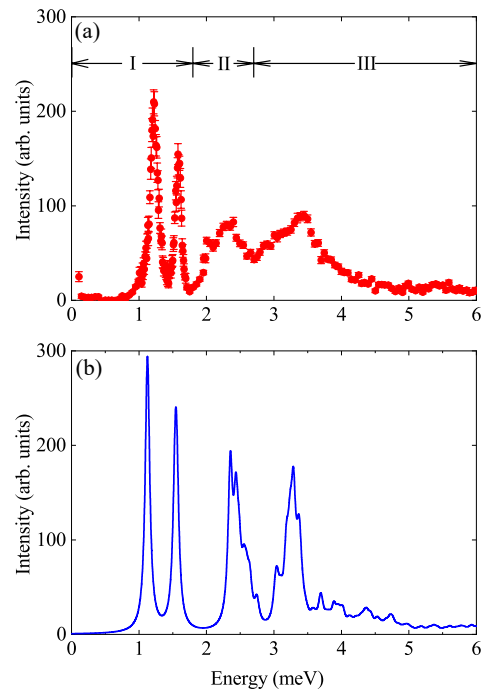


FIG. 2. Comparison of the spectral weight at the M point between the numerical calculation and the INS measurement. (a) INS intensity for $\text{Ba}_3\text{CoSb}_2\text{O}_9$, reproduced using the data published in Ref. [12]. (b) Numerical results obtained with the same parameters used for Fig. 1.

W -like excitation modes are observed. These two modes are nearly energy degenerate at the M point, rendering a strong coupling between these two modes. This energy range already falls within the two magnon excitation continuum. In the high energy region $\omega > 2.7$ meV, a weak and smeared W -like dispersive continuum whose tails extend to energy as high as 6 meV. The energy levels, shown in Fig. 1(e), clearly become more densely packed in this energy range as an indication of excitation continuum. Many of them have invisible spectral weights. The intensity shows a relatively brighter spot at $\omega \sim 3.3$ meV around the M point.

By comparison with the INS measurement data [11, 12], shown in Fig. 1(d), we find that the numerical result agrees very well with the experimental one in the whole energy range. This is a surprising result considering that there is not any adjustable parameter used in the calculation. In the low-energy region, the calculated dispersion relations of the three magnon bands agree quantitatively with the measurement data (see Fig. S8 in Supplemental Material [39]). In the high-energy region, the INS spectrum looks more diffusive than our numerical result. However, this does not mean that there is no feature in the INS data. In fact, in addition to the two sharp magnon peaks observed in the low-energy region, two more peaks are observed in the high-energy spectra of INS at the M point [12]. Figure 2 compares theoretical

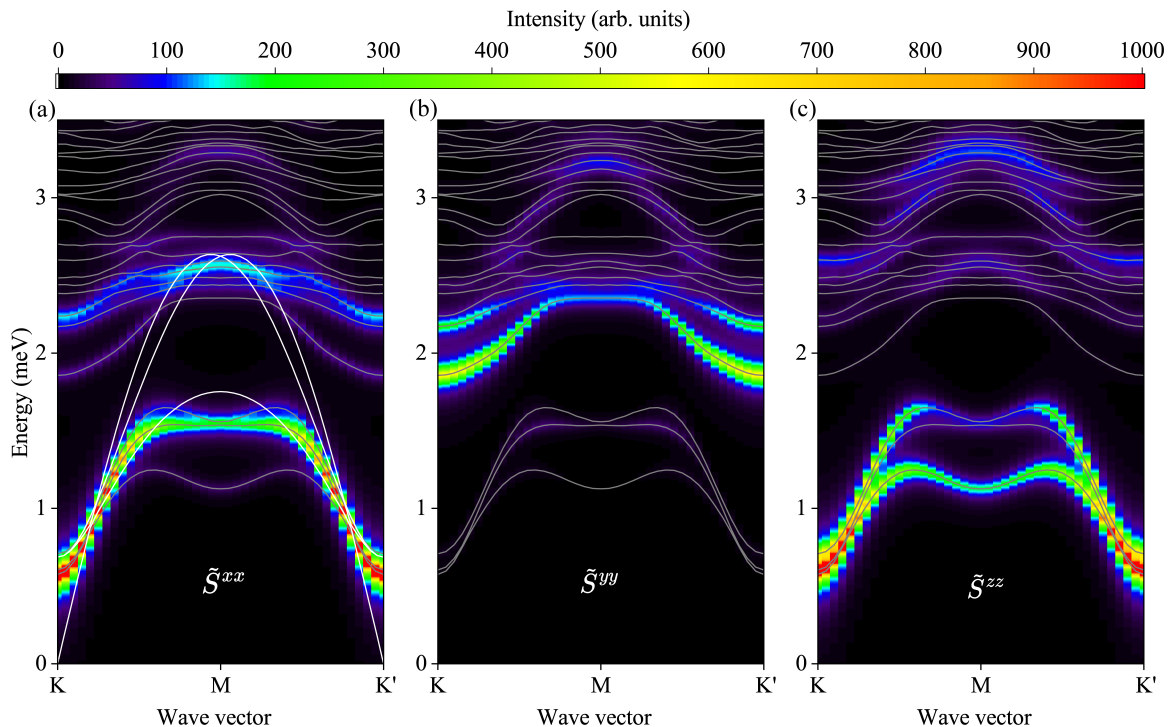


FIG. 3. Sublattice spectral function in the magnetic Brillouin zone. The momentum runs along the primary vectors of the magnetic Brillouin zone that is equivalent to the path $K - M - K'$ in the original Brillouin zone. The longitudinal direction is defined along the direction of the magnetization of sublattice A , i.e. along the y axis. (a) In-plane transverse fluctuation modes \tilde{S}^{xx} . (b) Longitudinal fluctuation modes \tilde{S}^{yy} . (c) Out-of-plane transverse fluctuation modes \tilde{S}^{zz} . The gray curves show the energy dispersions of the excited states. The energy dispersions of magnons predicted by LSWT (white curves) are also shown in (a) for comparison.

results for the energy dependence of the intensity with the experimental one at that point [12]. Again, the four-peak spectrum with the peak energies obtained from the numerical calculation agrees well with the experimental ones. This is the first time the two broad spectral peaks above 2 meV are disclosed in a theoretical calculation. The two high-energy INS peaks are broader than the numerical ones. In Sec.V in Supplemental Material [39], we present a detailed analysis of the bond-dimension dependence of the spin excitation spectra and find that these peaks are qualitatively unaltered and do not become significantly broadened with the increase of D . It suggests that the model Hamiltonian (1) captures the main features of the spin excitation spectra of $\text{Ba}_3\text{CoSb}_2\text{O}_9$ but is not sufficient to describe the diffusive INS spectra in the intermediate-energy scale. The derivation may result from the disorder, impurity, weak interlayer, or long-range interactions present in real materials but not included in the model Hamiltonian.

The projected spectra functions along the three principal axes, $S^{xx}(\mathbf{k}, \omega)$, $S^{yy}(\mathbf{k}, \omega)$ and $S^{zz}(\mathbf{k}, \omega)$, can be measured by utilizing spin-polarized neutrons. This provides a unique approach to experimentally test our numerical predictions shown in Figs. 1(e)-(g). As the magnetization is coplanar ordered, the low-energy spectral

weight of $S^{zz}(\mathbf{k}, \omega)$ contributes mainly from the out-of-plane transverse fluctuations. The low-energy spectral weights of $S^{xx}(\mathbf{k}, \omega)$ and $S^{yy}(\mathbf{k}, \omega)$, on the other hand, contribute from the in-plane transverse as well as longitudinal fluctuations.

To further elucidate the microscopic nature of low-energy excitations, we investigate the sublattice spectral functions in the framework of coordinates where all magnetic ordered spins are locally rotated toward the positive direction of the y -axis. We denote the corresponding spectral functions as $\tilde{S}^{xx}(\mathbf{k}, \omega)$, $\tilde{S}^{yy}(\mathbf{k}, \omega)$ and $\tilde{S}^{zz}(\mathbf{k}, \omega)$. In this case, $\tilde{S}^{yy}(\mathbf{k}, \omega)$ contributes mainly from the longitudinal fluctuations, and $\tilde{S}^{xx}(\mathbf{k}, \omega)$ and $\tilde{S}^{zz}(\mathbf{k}, \omega)$ contribute mainly from the in-plane and out-of-plane transverse fluctuations, respectively.

Figure 3 shows the numerical results for the three sublattice spectral functions (\tilde{S}^{xx} , \tilde{S}^{yy} , \tilde{S}^{zz}). Compared with the LSWT prediction (white curves in Fig. 3(a)), we find that the three magnon bands are strongly renormalized by their interaction with the high-energy continuum. For the three magnon bands below 1.8 meV, it is clear from Fig. 3(c) that the two bands whose energies are largest and smallest at the M point result predominantly from the out-of-plane transverse spin fluctuations. The third magnon band, whose energy lies between the other two

bands at the M point, apparently results mainly from the in-plane spin fluctuations.

In the intermediate-energy region $1.8 < \omega < 2.7$ meV, Fig. 3(b) clearly shows the two lowest-energy bands contribute mainly by the longitudinal spin fluctuations. This suggests that they are the damped Higgs modes, consistent with the prediction made based on the RVB picture [28]. It can be verified experimentally by taking spin-polarized neutron scattering measurements.

Figure 3 suggests that there is a significant transfer of spectral weights from the three low-energy magnon modes to the high-energy continuum. Such pronounced spectral weight transfer results inevitably from the interaction between the magnon excitations and the high-energy continuum. It leads to the downward bending of the three magnon bands around M , which implies that the interactions of these bands with other excitations around that point are very strong [12, 22, 27, 28]. As the spectral weight of the highest-energy magnon band is almost completely suppressed around the M point in all the directions, it further suggests that the downward bending of this band is not simply a consequence of the level repulsion imposed by high-energy excitation states. Otherwise, some remnant spectral weight from the original magnon band should be observed.

Discussion.— Our tensor network results reveal the key features of the dynamical spin spectra for the spin-1/2 antiferromagnetic Heisenberg model. Not only does it provide a good account for the INS spectrum of $\text{Ba}_3\text{CoSb}_2\text{O}_9$, but also a comprehensive picture for understanding dynamical couplings between different excitation modes without invoking any approximation that is not easy to control. Our result of the sublattice spin structure factors shows unambiguously that the lowest-energy band whose intensity is more pronounced around the K point in the intermediate-energy region contributes predominately by the longitudinal fluctuations, namely the Higgs modes. As the low-energy longitudinal fluctuations fall in the region of two-magnon continuum, their coupling with magnons leads to broadening of the Higgs peaks. The spectral peak around 2.3 meV in Fig. 2(a) at the M point, on the other hand, comes mainly from the in-plane transverse excitation mode, but strongly damped by its interaction with the Higgs mode. Besides, there are two kinds of transverse excitation modes, from the in-plane and out-of plane spin fluctuations, respectively. Their dynamical responses, as shown in Figs. 1(e)-(g), can be differentiated by taking INS measurements with polarized neutrons. Furthermore, we find that the spin excitation spectra weakly depend on the anisotropic parameter Δ (see Fig. S10 in Supplemental Material [39]).

This work demonstrates the great potential of the tensor network method in exploring the dynamic properties of highly frustrated antiferromagnets. It offers a new tool

to reveal the dynamic nature of exotic phases of quantum materials, such as quantum spin liquids and spin ices, and can be extended to study strongly correlated electronic systems [32]. Further improvement to the numerical results can be done by increasing the bond dimension of local tensors. This can increase the accuracy of the PEPS wave functions, especially for the low-energy excitation modes with long correlation lengths, and improve the energy resolution of dynamical correlation functions.

We thank Tao Li, Chun Zhang, Yi-Bin Guo and Xuan Li for helpful discussions. We thank Hidekazu Tanaka for providing the reference data. This work is supported by the National Key Research and Development Project of China (Grant No. 2017YFA0302901), the National Natural Science Foundation of China (Grants No. 11888101, No. 11874095, and No. 11974396), the Youth Innovation Promotion Association CAS (Grant No. 2021004), and the Strategic Priority Research Program of Chinese Academy of Sciences (Grants No. XDB33010100 and No. XDB33020300).

* These authors contributed equally to this work

† navyphysics@iphy.ac.cn

‡ txiang@iphy.ac.cn

- [1] P. Anderson, Mater. Res. Bull. **8**, 153 (1973).
- [2] L. Balents, Nature (London) **464**, 199 (2010).
- [3] Y. Zhou, K. Kanoda, and T.-K. Ng, Rev. Mod. Phys. **89**, 025003 (2017).
- [4] H. J. Liao, Z. Y. Xie, J. Chen, Z. Y. Liu, H. D. Xie, R. Z. Huang, B. Normand, and T. Xiang, Phys. Rev. Lett. **118**, 137202 (2017).
- [5] C. Castelnovo, R. Moessner, and S. L. Sondhi, Nature **451**, 42 (2008).
- [6] P. Fazekas and P. W. Anderson, Philos. Mag. **30**, 423 (1974).
- [7] D. A. Huse and V. Elser, Phys. Rev. Lett. **60**, 2531 (1988).
- [8] L. Capriotti, A. E. Trumper, and S. Sorella, Phys. Rev. Lett. **82**, 3899 (1999).
- [9] S. R. White and A. L. Chernyshev, Phys. Rev. Lett. **99**, 127004 (2007).
- [10] J. Ma, Y. Kamiya, T. Hong, H. B. Cao, G. Ehlers, W. Tian, C. D. Batista, Z. L. Dun, H. D. Zhou, and M. Matsuda, Phys. Rev. Lett. **116**, 087201 (2016).
- [11] S. Ito, N. Kurita, H. Tanaka, S. Ohira-Kawamura, K. Nakajima, S. Itoh, K. Kuwahara, and K. Kakurai, Nat. Commun. **8**, 235 (2017).
- [12] D. Macdougall, S. Williams, D. Prabhakaran, R. I. Bewley, D. J. Voneshen, and R. Coldea, Phys. Rev. B **102**, 064421 (2020).
- [13] T. Susuki, N. Kurita, T. Tanaka, H. Nojiri, A. Matsuo, K. Kindo, and H. Tanaka, Phys. Rev. Lett. **110**, 267201 (2013).
- [14] D. Yamamoto, G. Marmorini, and I. Danshita, Phys. Rev. Lett. **114**, 027201 (2015).
- [15] Y. Shirata, H. Tanaka, A. Matsuo, and K. Kindo, Phys. Rev. Lett. **108**, 057205 (2012).
- [16] G. Koutroulakis, T. Zhou, Y. Kamiya, J. D. Thompson,

- H. D. Zhou, C. D. Batista, and S. E. Brown, *Phys. Rev. B* **91**, 024410 (2015).
- [17] W. Zheng, J. O. Fjarestad, R. R. P. Singh, R. H. McKenzie, and R. Coldea, *Phys. Rev. B* **74**, 224420 (2006).
- [18] O. A. Starykh, A. V. Chubukov, and A. G. Abanov, *Phys. Rev. B* **74**, 180403 (2006).
- [19] A. L. Chernyshev and M. E. Zhitomirsky, *Phys. Rev. B* **79**, 144416 (2009).
- [20] M. Mourigal, W. T. Fuhrman, A. L. Chernyshev, and M. E. Zhitomirsky, *Phys. Rev. B* **88**, 094407 (2013).
- [21] A. V. Syromyatnikov, arXiv:2107.00256.
- [22] R. Verresen, R. Moessner, and F. Pollmann, *Nat. Phys.* **15**, 750 (2019).
- [23] A. Mezio, C. N. Sposetti, L. O. Manuel, and A. E. Trumper, *Europhys. Lett.* **9** **94**, 47001 (2011).
- [24] E. A. Ghioldi, A. Mezio, L. O. Manuel, R. R. P. Singh, J. Oitmaa, and A. E. Trumper, *Phys. Rev. B* **91**, 134423 (2015).
- [25] E. A. Ghioldi, M. G. Gonzalez, S.-S. Zhang, Y. Kamiya, L. O. Manuel, A. E. Trumper, and C. D. Batista, *Phys. Rev. B* **98**, 184403 (2018).
- [26] S.-S. Zhang, E. A. Ghioldi, Y. Kamiya, L. O. Manuel, A. E. Trumper, and C. D. Batista, *Phys. Rev. B* **100**, 104431 (2019).
- [27] F. Ferrari and F. Becca, *Phys. Rev. X* **9**, 031026 (2019).
- [28] C. Zhang and T. Li, *Phys. Rev. B* **102**, 075108 (2020).
- [29] F. Verstraete and J. I. Cirac, arXiv:cond-mat/0407066.
- [30] R. Orús, *Nat. Rev. Phys.* **1**, 538 (2019).
- [31] H.-J. Liao, J.-G. Liu, L. Wang, and T. Xiang, *Phys. Rev. X* **9**, 31041 (2019).
- [32] B. Ponsioen, F. F. Assaad, and P. Corboz, *SciPost Phys.* **12**, 6 (2022).
- [33] Y. Doi, Y. Hinatsu, and K. Ohoyama, *J. Condens. Matter Phys.* **16**, 8923 (2004).
- [34] Y. Kamiya, L. Ge, T. Hong, Y. Qiu, D. L. Quintero-Castro, Z. Lu, H. B. Cao, M. Matsuda, E. S. Choi, C. D. Batista, M. Mourigal, H. D. Zhou, and J. Ma, *Nat. Commun.* **9**, 2666 (2018).
- [35] R. P. Feynman, *Phys. Rev.* **94**, 262 (1954).
- [36] S. Östlund and S. Rommer, *Phys. Rev. Lett.* **5**, 3537 (1995).
- [37] J. Haegeman, B. Pirvu, D. J. Weir, J. I. Cirac, T. J. Osborne, H. Verschelde, and F. Verstraete, *Phys. Rev. B* **85**, 100408 (2012).
- [38] L. Vanderstraeten, M. Mariën, F. Verstraete, and J. Haegeman, *Phys. Rev. B* **92**, 201111 (2015).
- [39] See Supplemental Material for details, which includes Refs. [4,8,12,22,31,32,35-38,40-44].
- [40] Y. Iqbal, W.J. Hu, R. Thomale, D. Poilblanc, and F. Becca, *Phys. Rev. B* **93**, 144411 (2016).
- [41] O. Gtze, J. Richter, R. Zinke, and D. J. J. Farnell, *J. Magn. Magn. Mater.* **397**, 333 (2016).
- [42] D. Heidarian, S. Sorella, and F. Becca, *Phys. Rev. B* **80**, 012404 (2009).
- [43] L. Vanderstraeten, J. Haegeman and F. Verstraete, *Phys. Rev. B* **99**, 165121 (2019).
- [44] A. L. Chernyshev and M. E. Zhitomirsky, *Phys. Rev. Lett.* **97**, 207202 (2006).

Supplementary material

Spin Excitation Spectra of Anisotropic Spin-1/2 Triangular Lattice Heisenberg Antiferromagnets

Runze Chi,^{1,2,*} Yang Liu,^{1,2,*} Yuan Wan,^{1,3} Hai-Jun Liao,^{1,3,†} and T. Xiang^{1,2,4,‡}

¹Beijing National Laboratory for Condensed Matter Physics and Institute of Physics,
Chinese Academy of Sciences, Beijing 100190, China.

²School of Physical Sciences, University of Chinese Academy of Sciences, Beijing 100049, China.

³Songshan Lake Materials Laboratory, Dongguan, Guangdong 523808, China.

⁴Beijing Academy of Quantum Information Sciences, Beijing, China.

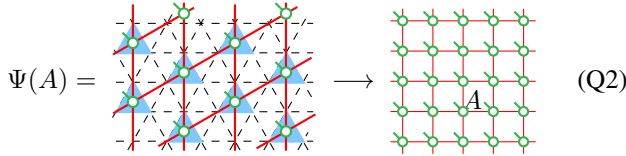
I. TENSOR NETWORK REPRESENTATION OF THE GROUND STATE

To simulate the magnetic excitations of $\text{Ba}_3\text{CoSb}_2\text{O}_9$, we need to calculate the zero-temperature dynamical spectral function

$$\begin{aligned} S^{\alpha\beta}(\mathbf{k}, \omega) &= \langle 0 | S_{-\mathbf{k}}^\alpha \delta(\omega - H + E_0) S_{\mathbf{k}}^\beta | 0 \rangle \\ &= \sum_m \langle 0 | S_{-\mathbf{k}}^\alpha | m \rangle \langle m | S_{\mathbf{k}}^\beta | 0 \rangle \delta(\omega - E_m + E_0), \quad (\text{Q1}) \end{aligned}$$

where H is the Hamiltonian, $\alpha, \beta = x, y, z$ are the spin components. $|m\rangle$ represents either the ground state if $m = 0$ or an excited state if $m \neq 0$. E_m is the corresponding energy eigenvalue.

In our calculation, the ground state $|0\rangle \equiv |\Psi(A)\rangle$ is represented by an infinite projected entangled-pair state (iPEPS) on a deformed square lattice, which is obtained from the original triangular lattice by grouping three sites on a triangle into one site



$$\Psi(A) = \text{[Diagram]} \quad (\text{Q2})$$

Local tensor A is assumed to be translation invariant. It contains three physical spins and is determined by variationally minimizing the ground state energy. This minimization is implemented by making use of the automatic differentiation [R1]. An accurate determination of local tensor A is crucial to the calculation of excitation spectra.

Once obtaining the optimized local tensors, we evaluate the expectation value of a physical observable by contracting the tensor-network states using the corner-transfer-matrix renormalization group (CTMRG). The result such obtained depends on both the bond dimension of the iPEPS, D , and the boundary bond dimension of CTMRG, χ . To obtain a better estimation of the expectation value, we extrapolate the results

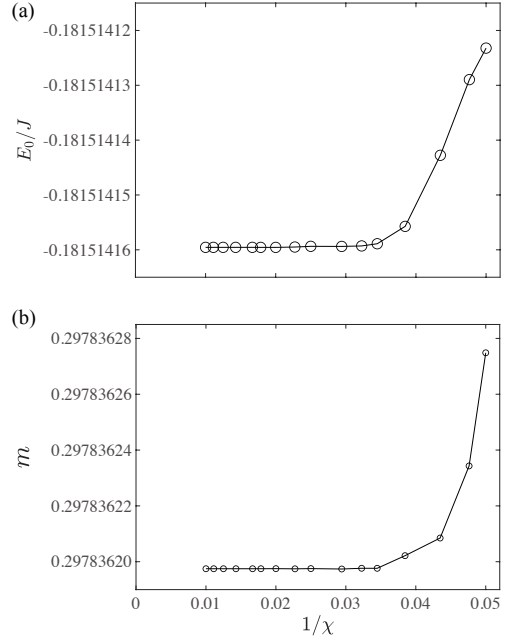


FIG. S1. The ground state energy E_0 (a) and the magnetization m (b) as functions of $1/\chi$ for the isotropic TLAHFM ($\Delta = 1.0$). The bond dimension of iPEPS $D = 4$.

first to the limit $1/\chi \rightarrow 0$ for a given D and then to the limit $1/D \rightarrow 0$.

Figure S1 shows how the ground state energy E_0 and the magnetization m converge with $1/\chi$ for the isotropic Heisenberg model obtained with the $D = 4$ iPEPS. In general, the CTMRG results should converge when χ becomes sufficiently greater than D^2 . This is indeed what we find from Fig. S1. By extrapolating the results to the limit $1/\chi \rightarrow 0$, we obtain the values of the ground state energy $E_0(D)$ and the magnetization $m(D)$ at a given D .

After obtaining the extrapolation values in the limit $\chi \rightarrow \infty$, we extrapolate E_0 and m with respect to $1/D$. Fig. S2 shows how the ground state energy and the magnetization converge with $1/D$ for both isotropic and anisotropic triangular-lattice antiferromagnetic Heisenberg models (TLAFHM). By fitting the iPEPS data with a power-law formula $E_0(D) = e_0 + aD^{-\alpha}$, we find that $E_0(\Delta = 0.95) = -0.1811J$ and $E_0(\Delta = 1.0) = -0.1840J$. For the isotropic TLAHFM with $\Delta = 1.0$, our result agrees with the DMRG result $-0.1837(7)J$ [R2] as well as the Coupled Cluster result

* These authors contributed equally to this work

† navyphysics@iphy.ac.cn

‡ txiang@iphy.ac.cn

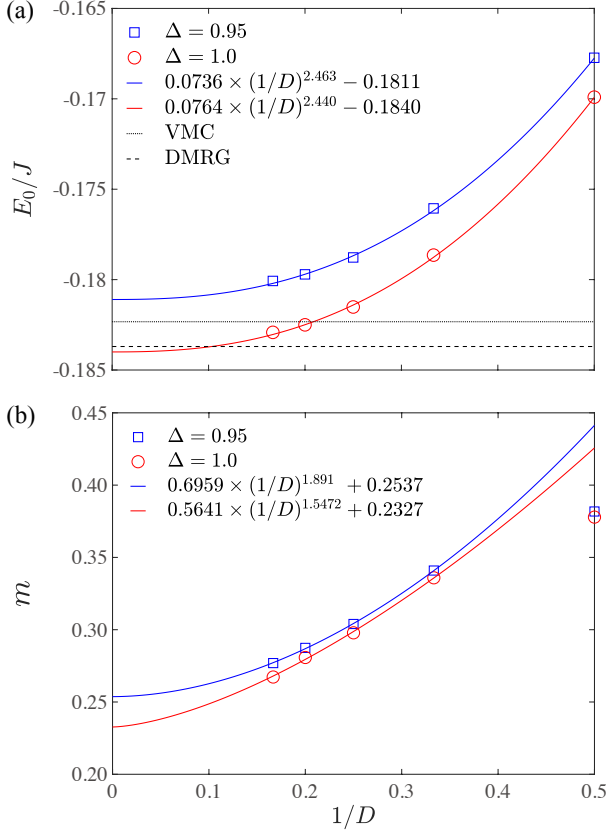


FIG. S2. Inverse bond-dimension dependences of (a) the ground state energy E_0 and (b) the magnetization m for the anisotropic (blue square, $\Delta = 0.95$) and isotropic (red circle, $\Delta = 1.0$) TLA FHM. The ground state energies obtained from DMRG [R2] and VMC [R4] are shown in panel (a) for comparison.

$-0.1838J$ [R3], and is lower than the variational Monte Carlo (VMC) result $-0.18233(3)J$ [R4] and the Green function Monte Carlo result $-0.18193(3)$ [R5]. It suggests that $\Psi(A)$ presents an accurate representation of the ground state of TLA FHM.

Similarly, we find that the magnetization also shows a power-law dependence on D , $m(D) = m_0 + bD^{-\beta}$. By fitting, we find that the extrapolated magnetization in the limit $1/D \rightarrow 0$ is $m_0 = 0.2537$ and $m_0 = 0.2327$ for the model with $\Delta = 0.95$ and 1.0 , respectively. The magnetization m_0 of the anisotropic TLA FHM ($\Delta = 0.95$) is slightly greater than the isotropic one ($\Delta = 1.0$) because the easy-plane anisotropy favors more strongly the coplanar 120° ordered ground state.

II. CALCULATION OF THE EXCITATION SPECTRUM

In the framework of tensor-network states, an excited state $|m\rangle$ is described by a tangent vector that is perpendicular to the ground state under the single-mode approximation [R6]. More specifically, $|m\rangle$ is obtained in two steps. First, we replace the local tensor A at site \mathbf{r} in $|\Psi(A)\rangle$ with a new tensor

B and denote it as $|\Phi_{\mathbf{r}}(B)\rangle$,

$$\Phi_{\mathbf{r}}(B) = \begin{array}{c} \text{---} \\ \text{---} \\ \text{---} \\ \text{---} \\ \text{---} \end{array} \begin{array}{c} \text{---} \\ \text{---} \\ \text{---} \\ \text{---} \\ \text{---} \end{array} \quad (Q3)$$

Second, we boost $|\Phi_{\mathbf{r}}(B)\rangle$ into a momentum eigenstate:

$$|\Phi_{\mathbf{k}}(B)\rangle = \sum_{\mathbf{r}} e^{i\mathbf{k}\cdot\mathbf{r}} |\Phi_{\mathbf{r}}(B)\rangle. \quad (Q4)$$

This single-mode approximated wave function was first introduced in the framework of matrix product states (MPS) by Ostlund and Rommer in one dimension [R7, R8]. It was extended to PEPS in two dimensions by Vanderstraeten *et al.* [R9].

The excited states such defined are the momentum eigenstates. They should be orthogonal to the ground state. This requires that $|\Phi_{\mathbf{r}}(B)\rangle$ be a vector in the tangent space of the ground state, satisfying the constraint

$$\langle \Phi_{\mathbf{r}}(B^\dagger) | \Psi(A) \rangle = 0. \quad (Q5)$$

Furthermore, it is simple to show that $|\Phi_{\mathbf{k}}(B)\rangle$ is invariant under the gauge transformation [R9]

$$B \rightarrow B + e^{i\mathbf{k}} AX - XA, \quad (Q6)$$

where X is an arbitrary $D \times D$ bond matrix. This implies that $|\Phi_{\mathbf{k}}(B)\rangle$ is a null tensor network state if B takes the value

$$B_X = e^{i\mathbf{k}} AX - XA. \quad (Q7)$$

Thus to determine the physically allowed B -tensors in the tangent space, one should exclude the tensors in the subspace spanned by all linearly independent B_X -tensors. This step is important to ensure the stability of the effective norm matrix N^{eff} , defined by Eq. (Q8), in solving the generalized eigen-equation (Q14). As a PEPS has two perpendicular bond directions, there are $2D^2 + 1$ linearly independent B -tensors that should be excluded.

To find the excited states, we start from all physically allowed and orthogonal B -tensors, denoted as \tilde{B}_m , in the tangent space of the ground state. The norm matrix is defined by the wave function overlap between different tangent vectors

$$N_{mn}^{\text{eff}} = \langle \Phi_{\mathbf{k}}(\tilde{B}_m^\dagger) | \Phi_{\mathbf{k}}(\tilde{B}_n) \rangle. \quad (Q8)$$

The corresponding Hamiltonian matrix is

$$H_{mn}^{\text{eff}} = \langle \Phi_{\mathbf{k}}(\tilde{B}_m^\dagger) | H | \Phi_{\mathbf{k}}(\tilde{B}_n) \rangle. \quad (Q9)$$

Since N_{mn}^{eff} and H_{mn}^{eff} are linear functions of local tensor \tilde{B}_m^\dagger and \tilde{B}_n , they can also be written as

$$N_{mn}^{\text{eff}} = \tilde{B}_m^\dagger \mathbb{N}_{\mathbf{k}} \tilde{B}_n, \quad H_{mn}^{\text{eff}} = \tilde{B}_m^\dagger \mathbb{H}_{\mathbf{k}} \tilde{B}_n, \quad (Q10)$$

where $\mathbb{N}_{\mathbf{k}}$ and $\mathbb{H}_{\mathbf{k}}$ are $M \times M$ matrices.

As $\mathbb{N}_{\mathbf{k}}$ and $\mathbb{H}_{\mathbf{k}}$ do not explicitly depend on \tilde{B} -tensors, the above expression suggests that both $\mathbb{N}_{\mathbf{k}}\tilde{B}_n$ and $\mathbb{H}_{\mathbf{k}}\tilde{B}_n$ can be determined by simply taking the derivative of the diagonal term of the norm matrix N_{nn}^{eff} and effective Hamiltonian H_{nn}^{eff} with respect to \tilde{B}_n^\dagger , respectively,

$$\left(\mathbb{N}_{\mathbf{k}}\tilde{B}_n\right) = \frac{\partial}{\partial \tilde{B}_n^\dagger} \left(\tilde{B}_n^\dagger \mathbb{N}_{\mathbf{k}} \tilde{B}_n\right), \quad (\text{Q11})$$

$$\left(\mathbb{H}_{\mathbf{k}}\tilde{B}_n\right) = \frac{\partial}{\partial \tilde{B}_n^\dagger} \left(\tilde{B}_n^\dagger \mathbb{H}_{\mathbf{k}} \tilde{B}_n\right). \quad (\text{Q12})$$

The above derivatives, as discussed in Ref. [R11], can be evaluated by utilizing the automatic differentiation [R1]. From these derivatives, we can obtain all the matrix elements of N_{mn}^{eff} and H_{mn}^{eff} , namely,

$$N_{mn}^{\text{eff}} = \tilde{B}_m^\dagger \left(\mathbb{N}_{\mathbf{k}}\tilde{B}_n\right), \quad H_{mn}^{\text{eff}} = \tilde{B}_m^\dagger \left(\mathbb{H}_{\mathbf{k}}\tilde{B}_n\right). \quad (\text{Q13})$$

By solving the following generalized eigen-equation,

$$\sum_n H_{mn}^{\text{eff}} v_{np} = \sum_n E_p N_{mn}^{\text{eff}} v_{np}. \quad (\text{Q14})$$

we obtain the B -tensor of the m th excited state

$$B_m = \sum_n \tilde{B}_n v_{nm}, \quad (\text{Q15})$$

and the corresponding excitation energy E_m . Finally, we can use these results to calculate the zero-temperature dynamical spectral function (Q1).

The main computational cost is to evaluate the derivative of H_{nn}^{eff} for each independent excited basis state, which scales as $O(D^{12})$ [R1, R11]. For each momentum point \mathbf{k} , the total computational cost scales as $O(\mathcal{N} \times D^{12})$, where $\mathcal{N} \sim dD^4 - 2D^2 - 1$ is the total number of excited basis states and d is the physical bond dimension.

III. SUM RULE OF THE DYNAMICAL SPECTRAL FUNCTION

After obtaining the wave functions of the excitation states, we can calculate the dynamical spectral function using the formula

$$S^{\alpha\alpha}(\mathbf{k}, \omega) = \sum_m w_{\mathbf{k}}^\alpha(m) \delta(\omega - E_m + E_0), \quad (\text{Q16})$$

where

$$w_{\mathbf{k}}^\alpha(m) = \left| \langle \Phi_{\mathbf{k}}(B_m^\dagger) | S_{\mathbf{k}}^\alpha | \Psi(A) \rangle \right|^2 \quad (\text{Q17})$$

is the spectral weight, and the delta function is expanded by a Lorentzian broadening factor η , which mimics the finite temperature broadening effect for spectra function.

If the single-spin excited states $|\Phi_{\mathbf{k}}(B_m)\rangle$ are complete, it is expected that the dynamical spectral function should satisfy the following sum rule

$$\sum_{m,\alpha} w_{\mathbf{k}}^\alpha(m) = \sum_{\alpha} \left[\langle 0 | S_{-\mathbf{k}}^\alpha S_{\mathbf{k}}^\alpha | 0 \rangle - |\langle 0 | S_{\mathbf{k}}^\alpha | 0 \rangle|^2 \right]. \quad (\text{Q18})$$

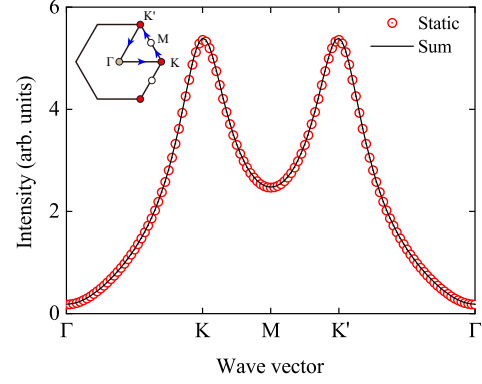


FIG. S3. Verification of the sum rule for the dynamical spectral function. Comparison of the total spectral weights (black curve) with the static spin structure factor (red circles) along the momentum path $\Gamma - K - M - K' - \Gamma$.

The right hand side of this equation is the static spin structure factor, which is determined purely by the ground state wave function $|\Psi(A)\rangle$.

Fig. S3 compares the total spectral weights with the static spin structure factor along the momentum path $\Gamma - K - M - K' - \Gamma$. Clearly, the sum rule is satisfied.

IV. BASIS NUMBER DEPENDENCE OF SPIN EXCITATION SPECTRA

The solution of the generalized eigenequation (Q14) may become unstable if the norm matrix is ill-conditioned. This instability can be removed if we can eliminate all redundant gauge degrees of freedom, including the null modes, in $|\Phi_{\mathbf{k}}(B)\rangle$ and reduce the numerical error in the normal matrix N^{eff} to a sufficiently low level. For the $D = 2$ case, we indeed

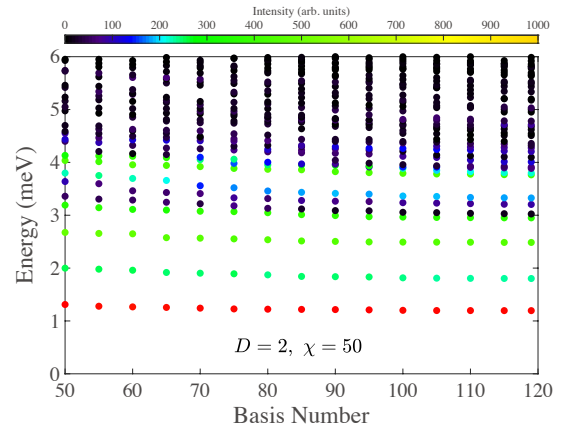


FIG. S4. Dependence of the spin excitation spectra on the basis number of the norm matrix for the anisotropic TLAFHM ($\Delta = 0.95$) at the M point obtained with the $D = 2$ PEPS wave function. $\chi = 50$ is used in the CTMRG contraction. The color denotes the spectral weight.

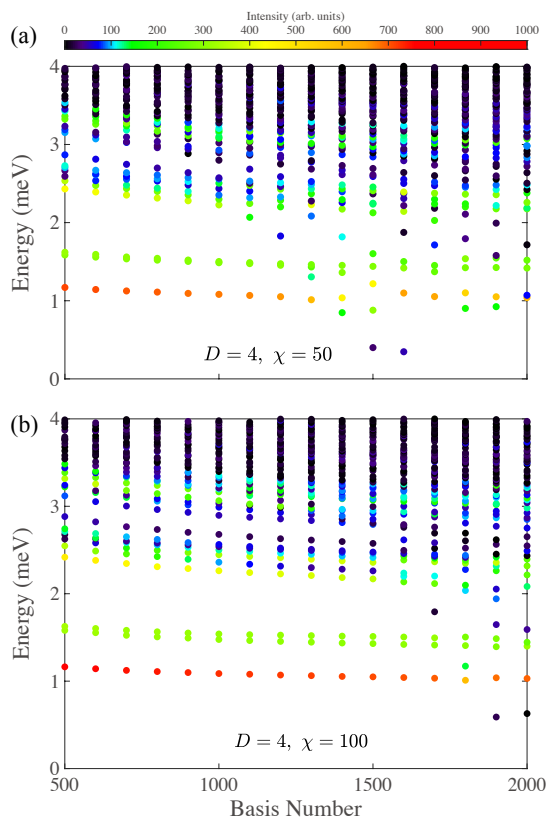


FIG. S5. Excitation spectra of the anisotropic TLAHFM ($\Delta = 0.95$) as a function of the basis number of the norm matrix for the $D = 4$ state at the M point. The boundary bond dimension used by CTMRG is (a) $\chi = 50$ and (b) $\chi = 100$. The color denotes the spectral weight.

find that there is no instability in the calculation.

Figure S4 shows how the excitation spectra vary with the basis number of the norm matrix used for solving the generalized eigen-equation at the M point for the $D = 2$ state. The norm matrix is calculated with high precision by utilizing a relatively large $\chi = 50$. The converged behavior of the spectra with the basis number of the norm matrix indicates that the $D = 2$ norm matrix is well-conditioned after removing all the null modes.

However, it is generally quite difficult to calculate very accurately the norm matrix by employing CTMRG or the boundary MPS when D becomes larger than 2. If the norm matrix is not that accurately calculated, it may still become ill-conditioned no matter if the null modes are removed or not [R10, R11]. To remove this instability, one has to take a lower rank approximation for the norm matrix by discarding its ill-conditioned eigenvalues.

Figure S5 shows how the spectra vary with the basis number of the norm matrix retained for the $D = 4$ state at the M point. The dimension of the norm matrix is about 2000 when $D = 4$. In case the boundary bond dimension $\chi = 50$, Fig. S5 (a), some spurious eigenlevels begin to appear in the excitation spectrum when the basis number is greater than 1100. Reducing the error in the norm matrix by increasing χ to 100,

we find that the number of ill-conditioned eigenvalues is also dramatically reduced. In this case, the instability in the excitation spectra occurs only when the basis number becomes larger than 1700 (Fig. S5 (b)). It shows that the accuracy of the norm matrix is a vital control parameter for resolving the ill-condition problem.

Moreover, we find that the accuracy of the norm matrix evaluated with CTMRG depends strongly on the size of the unit cell in the ground state iPEPS. The smaller the unit cell, the higher the accuracy of the norm matrix if the same number of boundary basis states χ are used in the CTMRG calculations. For this reason, we adopt the iPEPS ansatz (Q1), whose size of the unit cell is 1, by grouping three inequivalent spins together.

V. BOND DIMENSION DEPENDENCY OF SPIN EXCITATION SPECTRA

Now let us consider how fast the spin excitation spectra converge with the bond dimensions χ and D for the $\Delta = 0.95$ TLAHFM.

Figure S6 shows the $D = 4$ spectral function at the M point obtained by CTMRG with three different $\chi = 50, 70$ and 100 and two Lorentzian broadening parameters $\eta = 0.04$ and 0.1 meV. If a small Lorentzian broadening parameter η is used ($\eta = 0.04$ meV, which equals ≈ 0.46 Kelvin, lower than the measured temperature 1.7 Kelvin of the neutron scattering

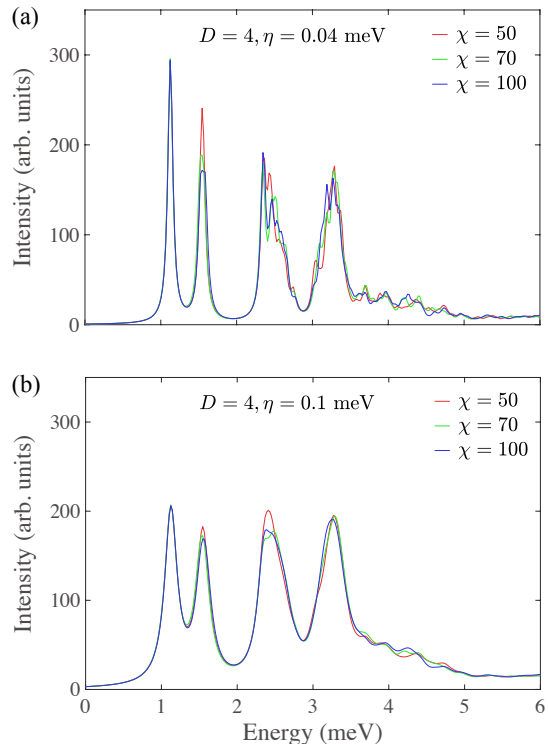


FIG. S6. Comparison of the spectral functions at M point obtained with three different $\chi = 50, 70$ and 100 and two Lorentzian broadening parameters $\eta = 0.04$ meV in (a) and 0.1 meV in (b).

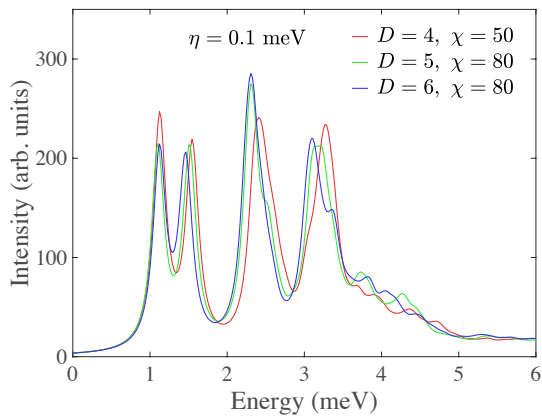


FIG. S7. Spectral functions at the M point obtained from the $D = 4, 5$ and 6 PEPS.

experiment [R12]), there are small fluctuations in the high-energy peaks. On the other hand, if we set $\eta = 0.1$ meV (≈ 1.16 Kelvin, closer to the measurement temperature), we find that the four peaks converge quite well with the increase of χ . It suggests that the energy error of our numerical results for the $D = 4$ case is roughly about 0.1 meV, higher than 0.04 meV.

Figure S7 compares the spectral functions at the M point obtained using the $D = 4, 5$ and 6 PEPS wave functions. The four-peak structures are observed in all the cases. Only the peak energies are slightly moved with the bond dimension D . Hence, the key features of the spin excitation spectra we obtained are intrinsic properties of TLA FHM.

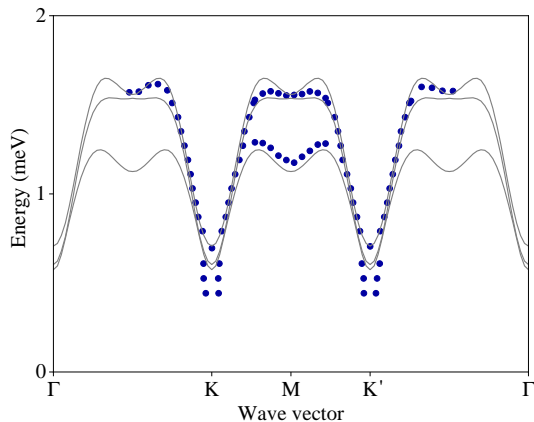


FIG. S8. Comparison of the numerical results (gray curves) of the energy dispersion relations of the three magnon bands with the experimental ones (blue dots). The experimental results are reproduced from the data published in the supplemental materials of Ref. [R12].

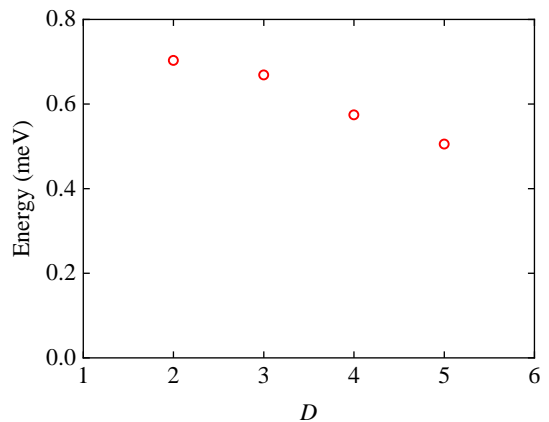


FIG. S9. Minimal spectral gap as a function of bond dimension D . The lowest spectral gap of the XXZ model occurs at the K point (see. Fig. S8) in the Brillouin zone. The gap values are obtained by contracting the effective Hamiltonian tensor network states of the excited states using the corner transfer matrix renormalization group method with a bond dimension $\chi = 50$ for $D = 2, 3, 4$ and $\chi = 60$ for $D = 5$.

VI. ENERGY DISPERSION OF THE THREE MAGNON BANDS

The lowest three excitation bands shown in Fig. 1.c in the main text are the three magnon bands. Fig. S8 compares the numerical results for the energy dispersion of these bands with the experimental data [R12]. Our results agree with the experimental ones, except the low-energy spectra around the K point associated with the gapless Goldstone mode. In the PEPS representations, the excitation is always gapped if D is finite. The gap vanishes only in the limit $D \rightarrow \infty$. At any finite D , it is expected that the minimal excitation gap should decrease with the increase of D . This, as shown in Fig. S9, is indeed what we see in our calculation. In principle, the energy gap should converge with D in certain power law for sufficiently large D in a gapless system [R13]. As the values of D that were used in our calculation are still very small, our data have not yet entered this power-law converged regime.

VII. INTERACTION ANISOTROPY DEPENDENCY OF SPIN EXCITATION SPECTRA

Linear spin wave theory predicts that the spin excitation spectra of TLA FHM heavily depend on the anisotropy Δ (see Fig. S10 (d-f)). In particular, the $1/S$ nonlinear spin wave theory (NLSW) [R14] suggested that the anisotropy may cause an instability in the low-energy magnon spectra due to the spontaneous two-magnon decay. In particular, NLSW predicts that the magnon decay is kinematically allowed in a large portion of the Brillouin zone when $\Delta > 0.92$, whereas this instability disappears when $\Delta < 0.92$.

For $\text{Ba}_3\text{CoSb}_2\text{O}_9$, the anisotropic parameter Δ of is about 0.95 according to experimental measurements. Hence the low-energy magnon excitations of $\text{Ba}_3\text{CoSb}_2\text{O}_9$ should be

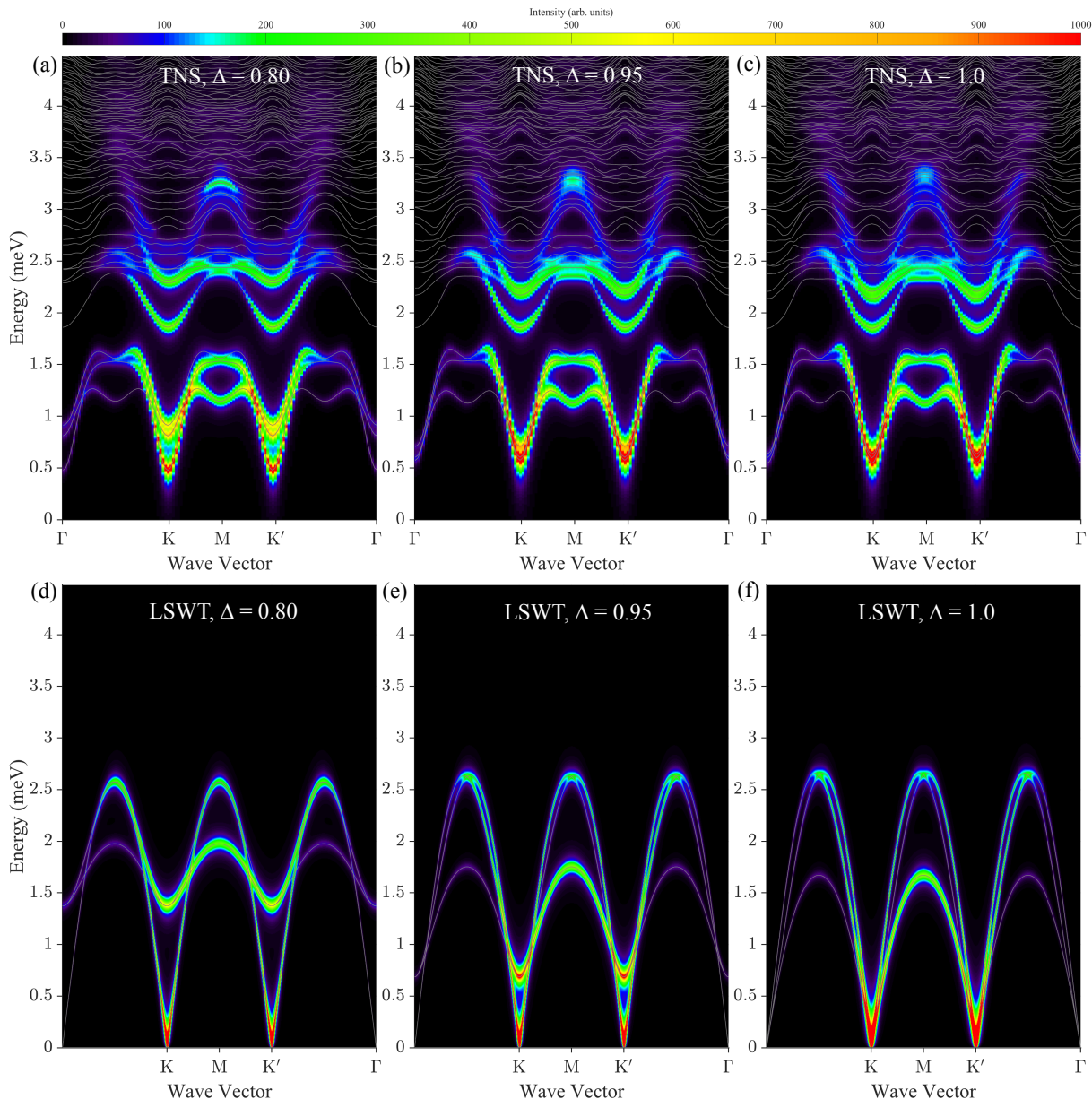


FIG. S10. Comparison of spin excitation spectra obtained using the tensor-network method (a-c) with those obtained by spin-wave theory (d-f) for TLAFHM with different anisotropic parameters $\Delta = 0.8, 0.95$, and 1.0 , respectively.

broadened due to finite lifetime caused by the magnon decay according to NLSW. However, the neutron scattering experiments observed sharp low-energy magnon excitations. This motivates us to investigate how the spin excitation spectra vary with the anisotropy.

We calculate the spin excitation spectra for the three representative cases with $\Delta = 0.8, 0.95$ and 1.0 , respectively. Different from the prediction of NLSW, our results show sharp low-energy magnon excitations for all the three cases (Fig. S10 (a-c)). Moreover, we find that the overall spectra, including the 'W'-like high-energy excitations and low-energy roton-like excitations, only slightly depend on the anisotropic values. Thus it strongly suggests that there is not an instability

caused by the two-magnon decay in the anisotropic TLAFHM with $0.8 \leq \Delta \leq 1$.

There are two main differences due to anisotropy. First, with the decrease of anisotropy, the excitation of the second and third low-energy magnons at the K point will gradually rise up, but the changes are significantly less than those predicted by the linear spin wave theory. Second, with the increase of anisotropy, the spectra at about 1.5 meV and 2.3 meV around the M point become more and more flat simultaneously, suggesting that there is a repulsive interaction between the high- and low-energy excitations. This is consistent with the picture of the avoided magnon decay due to level-continuum repulsion proposed in Ref. [R15].

-
- [R1] H.-J. Liao, J.-G. Liu, L. Wang, and T. Xiang, *Phys. Rev. X* **9**, 31041 (2019).
- [R2] Y. Iqbal, W.J. Hu, R. Thomale, D. Poilblanc, and F. Becca, *Phys. Rev. B* **93**, 144411 (2016).
- [R3] O. Götze, J. Richter, R. Zinke, and D. J. J. Farnell, *J. Magn. Mater.* **397**, 333 (2016).
- [R4] D. Heidarian, S. Sorella, and F. Becca, *Phys. Rev. B* **80**, 012404 (2009).
- [R5] L. Capriotti, A. E. Trumper, and S. Sorella, *Phys. Rev. Lett.* **82**, 3899 (1999).
- [R6] R. P. Feynman, *Phys. Rev.* **94**, 262 (1954).
- [R7] S. Östlund and S. Rommer, *Phys. Rev. Lett.* **75**, 3537 (1995).
- [R8] J. Haegeman, B. Pirvu, D. J. Weir, J. I. Cirac, T. J. Osborne, H. Verschelde, and F. Verstraete, *Phys. Rev. B* **85**, 100408 (2012).
- [R9] L. Vanderstraeten, M. Mariën, F. Verstraete, and J. Haegeman, *Phys. Rev. B* **92**, 201111 (2015).
- [R10] L. Vanderstraeten, J. Haegeman and F. Verstraete, *Phys. Rev. B* **99**, 165121 (2019).
- [R11] B. Ponsioen, F. F. Assaad, and P. Corboz, *SciPost Phys.* **12**, 6 (2022).
- [R12] D. Macdougall, S. Williams, D. Prabhakaran, R. I. Bewley, D. J. Voneshen, and R. Coldea, *Phys. Rev. B* **102**, 064421 (2020).
- [R13] H. J. Liao, Z. Y. Xie, J. Chen, Z. Y. Liu, H. D. Xie, R. Z. Huang, B. Normand, and T. Xiang, *Phys. Rev. Lett.* **118**, 137202 (2017).
- [R14] A. L. Chernyshev and M. E. Zhitomirsky, *Phys. Rev. Lett.* **97**, 207202 (2006).
- [R15] R. Verresen, R. Moessner, and F. Pollmann, *Nat. Phys.* **15**, 750 (2019).